# Fabrication of ZnO Thin Films from Nanocrvstal Inks

**Anthony J. Morfa,* Gary Beane,1 Benjamin Mashford,t Birendra Singh,* Enrico Della Gaspera,* Alex Martucci,* and Paul Mulvaney***

School of chemistry & Bio2l institute, University of Melbourne, Parkville, Victoria, so jo, Australia, CSJRO Division of Materials Science and Engineering, Clayton, Victoria, 3169, Australia, and Dipartimento di ingegneria Meccanica Settore Materiali, Università di Padova, Via Marzolc, 9, 35131 Padova, Italy

Received: July 28, 2010; Revised Manuscript Received: October 11, 2010

Zinc oxide nanocrystals were prepared in ethanol and spin-cast to form semiconductor nanocrystal thin films that were thermally annealed at temperatures between 100 and 800°C. Particle size. monodispersity, and film porosity were determined by X-ray diffraction, ultraviolet—visible absorption spectroscopy, and spectroscopic ellipsotnetry, respectively. Film porosity rapidly decreased above 400 °C, from 32% to 26%, which coincided with a change in electronic properties. Above 400 °C. the ZnO electron mobility, determined from FET transfer characteristics, increased from $l0^{-3}$ to $10^{-1}$ $cm^2$ V $s^{-1}$, while the surface resistivity. determined from electrical impedance, decreased from $10^7$ to $10^3$ Ω m over the same temperature range. Below the densification point, nanoparticle core resistivity was found to increase from $10^4$ to $10^6$ Ω m, which is caused by the increasing polydispersity in the quantized energy levels of the nanocrystals. From 100 to 800 °C, crystallite size was found to increase from 5 to 18 nm in diameter. The surface resistance was decreased dramatically by passivation with butane thiol.

## Introduction

Semiconductor nanocrystal thin films[1-3] are becoming increasingly prominent in thin-film electronics because of their low cost of fabrication and the tunability of their optoelectronic properties.[4-8] Although this tunability is desirable for certain applications, such as light-emitting diodes and photovoltaic devices, the creation of films from nanoparticle inks with bulk properties is also desirable, particularly for “printed electronics”.[9,10]

An important material in this respect is ZnO. Thin films of ZnO are used in transistors,115 as charge injection layers,[16,17] and as UV emitters, but these are currently produced primarily by chemical vapor deposition and sputtering methods.[18,10,19,20]

In order to utilize ZnO in “flexible electronics”, it would be useful to fabricate bulk ZnO films using low-temperature, wet- chemical methods. In this paper we present data on the synthesis of such ZnO films from nanocrystal inks. The key advantage of this approach is that films prepared from preformed crystalline ZnO particles will sinter to form semiconducting films at quite low temperatures, while conventional sol — gel methods require nucleation of ZnO from alkoxides, which occurs only at temperatures >500 °C. Various measurements are made at thermal annealing temperatures varying from 100 to 800 °C. With FTIR spectroscopy, the chemical composition of the material is determined. Spectroscopic ellipsometry is used to determine the porosity of the films, while UV absorption spectroscopy and X-ray diffraction measurements are used to determine the average crystallite size in the film at different annealing temperatures. The electrical impedance of the films was used to calculate the resistivity of ZnO thin films. Electron mobility was determined from field-effect transistor transfer characteristics of ZnO films. These results are correlated to show that film porosity and quality electronic materials from nanoparticle inks. We conclude that it is possible to create n-type ZnO with reasonable mobilities using nanocrystal inks at temperatures down to 200 °C, though optimal mobility and film quality are only achieved by annealing above 500 °C.

## Materials and Characterization

**Materials.** Nanoparticles of ZnO were prepared by the method outlined by Mashford[6] and others.[21,22] All solvents used were from Sigma-Aldrich. Zinc acetate dihydrate was dissolved in 75 mL of absolute ethanol at 40 °C to a total solute concentration of 58 m**M**. After the complete dissolution of zinc acetate, seven 200μm aliquots of 25% tetramethyl ammoniurn hydroxide (in methanol, from Sigma-Aldrich) were added over 120 s with vigorous stirring. The solution was immediately placed in a freezer maintained at —4 °C. Before casting films of ZnO, the stock solution was washed and concentrated. This was done by precipitation of the particles. Two milliliters of the stock ZnO colloid solution was precipitated by adding hexane dropwise and then redispersed in 150 μm of 1-propanol. This concentrated colloid solution was filtered through a Millipore (Millex PVDF) filter with a 220 nm pore size just before spin-casting.

Prepatterned ITO-on-glass electrodes (from Thin-Film Designs) were prepared via standard photolithography techniques using AZ Electronics 1518 photoresist. The ITO was etched using 60% HCI over 40 mm.

The ITO, quartz, and silicon substrates were cleaned using the same technique. Prior to ZnO film casting. each substrate was immersed first in acetone and then in isopropanol for 20 mm in a Unisonics ultrasonic bath. Each substrate was then blown dry using dry nitrogen.

Films were prepared by rapidly applying 50 μL of filtered ZnO solution to a substrate spinning at 1000 rpm on a Headway Research spin coater. The samples were spun for 30 s, with

* To whom corrcspondence should be addressed. E-mail: amorfa@gmail.com

* University of Melbourne.

* CSIRO Division of Materials Science and Engineering.

* Università di Padova.

10.1021/jp107043z © XXXX American Chemical Society

ZnO being applied in the first seconds. After the spin step was complete, the sample was moved to a benchtop to sit for 5 min before being placed in an MTI tube furnace for 30 min. Depending on the sample, the tube furnace temperature was set between 100 and 800 °C. Nitrogen was used to purge the furnace, with constant nitrogen flow maintained throughout heating to maintain a dust-free and oxygen deficient environment. For electronic measurements, two films were applied, each annealed after casting. This was found to prevent electronic shorting.

For the preparation of samples where, metal electrodes were necessary, gold or aluminum was used as received from Aldrich. The samples were masked using an appropriate shadow mask and placed in a Emitech K975 thermal evaporation chamber. The chamber pressure was lowered to below $10^{-3}$ mbar before evaporation of the metal. Metal films were deposited to a final film thickness of 100 nm.

Field-effect transistor samples were prepared on doped silicon wafers ($N \sim 3 \times 10^{17} cm^{-3}$, from Fraunhofer IMPS) with an $SiO_2$ layer of known thickness (230 nm). Aluminum source and drain contacts were then evaporated with a channel distance, *L, of 60 μm* and channel width, *W*, of 3 mm, through a laser milled shadow mask (MasterCut Technologies). Samples were kept in an inert atmosphere for testing to minimize the effect of oxygen on the contacts. Electrical, measurements were carried out on a Keithley 2612 source-measure-unit. Impedance measurements were made on an Autolab potentiostat and modeled in the accompanying FRA software. Values in this work are an average value, with typical sample sets being four samples on several substrates, with a standard deviation at or below 10%.

**Characterization.** The properties of the films were monitored optically and physically using several techniques. Samples for optical absorption (Cary 5) were prepared on quartz slides. Film volume was monitored using spectroscopic ellipsometry (JY Uvisel) and physical profilometry (Veeco Dektak 150). These samples were prepared on silicon wafers with a 2.6 nm native oxide layer. The films were characterized by X-ray diffraction using a Philips diffractometer equipped with glancing-incidence X-ray optics. The analysis was performed at 0.5° using Cu Kα Ni-filtered radiation at 30 kV and 40 mA. The average crystallite size was calculated from the Debye—Scherrer[23] equation after fitting the experimental profiles using the method described by Enzo et al.[24]

## Results

**Crystallite Growth.** X-ray diffraction patterns were collected from samples prepared on silicon wafers and annealed at temperatures ranging from 100 to 800 °C under nitrogen flow and are shown in Figure Ia. These measurements show that the particles prepared arc wurtzite ZnO with the {100}, {002},{101), and {102) diffraction orders clearly visible.[25] For samples that were annealed at temperatures up to 400 °C, the diffraction peaks are broad, with low intensity, indicating small crystallite sizes within the film. From 500 °C and above, the diffraction peaks become sharp and well-resolved indicating increased particle size. Using the Debye—Scherrer equation[23,24] (see eq 1), the average crystallite size can be calculated. In this equation, r is the mean crystallite size, $K$ is the shape factor (0.9 for spheres), λ is the X-ray wavelength (1.54 Å), $\beta$ is the line broadening at full width half-maximum intensity, and 0 is the Bragg angle. The crystallite size was calculated for each of the four peaks labeled in Figure 1a and the average values are shown in Figure 1b, with the error bars representing the standard

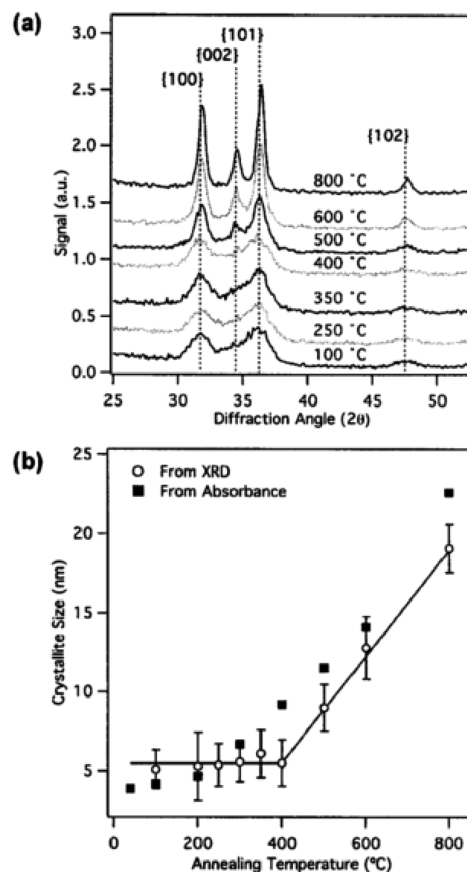


Figure 1. (a) X-ray diffraction patterns of ZnO films, prepared from nanoparticle solutions, annealed to temperatures ranging from 100 to 800 °C. (b) Average ZnO crystallite size in thin films prepared from nanoparticle inks, annealed to temperatures ranging from 1(X) to 800 °C. The sizes are determined from X-ray diffraction and absorbance data, where empty circles and filled squares represent the calculated size from each technique, respectively. The error shown for the XRD data represents the standard deviation in crystallite size of the four peaks shown in (a).

size remains constant at 5 nm until 400 °C at which point it begins to increase and reaches an average value of 19 nm at 800 °C.

$$\tau = \frac{K\lambda}{\beta \cos(\theta)} \quad (1)$$

deviation of these four values. The average crystallite

An increase in crystallite size with increasing temperature is supported by the measured absorption spectra shown in Figure 2a. The first exciton absorption peak red shifts with increased annealing temperature, indicating the average particle size increases with annealing temperature. Spanhel[22] et al. and Wood and colleagues[26] have calibrated the relationship between the energy of the first exciton absorption band and particle size for ZnO nanocrystals in ethanol, With these data, the particle size can be estimated from the spectra and it is evident that the particle size increases steadily with annealing temperature (see Figure 1b). Furthermore, the red shift of the absorption band is accompanied by a broadening of the first excitonic peak.

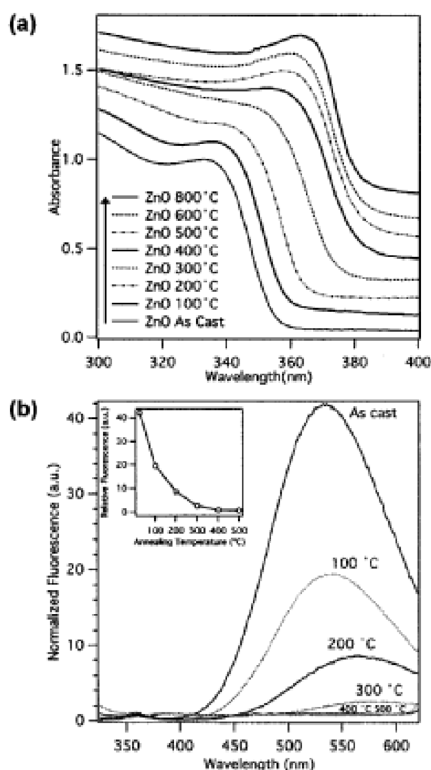


**Figure 2.** (a) ZnO thin-film absorbance as a function of thermal annealing. Samples were prepared on quartz and then annealed from 100 to 800 °C. A clear red shift is observed as films are annealed and the average crystallite size increases. (b) ZnO thin-film fluorescence for films annealed at temperatures ranging from 100 to 500 C. The inset shows the peak maximum plotted versus film thermal annealing temperature.

Eventually this becomes a broad shoulder, indicative of a highly polydisperse particle size distribution[27] within the film. The values presented in Figure la are estimates of particle size and not crystallite size. The observed differences between absorption-determined particle size and X-ray diffraction (XRD) determined crystallite size are to be expected for particles of low crystallinity.

ZnO nanoparticles prepared in ethanol exhibit a well-known defect fluorescence[28−30] that decreases with annealing in solvent.[26,31] ZnO nanoparticle films exhibit the same fluorescence as in solution (see Figure 2b), and the fluorescence intensity can likewise be reduced by thermal annealing. When the fluorescence spectra are normalized to the exciton emission, the relative change in surface defect emission can be compared between films of different thicknesses (the inset shows the defect-fluorescence maximum versus thermal annealing temperature). As the sample is annealed, the defect fluorescence decreases in intensity and red shifts. At 400 °C, the presence of defect emission is dramatically reduced compared to as-cast films, and by 500 °C, this emission is nonexistent.

**Chemical Characterization.**
The presence of chemical precursors can clearly be seen in the infrared transmission spectra (see Figure 3). These films were prepared via drop-casting, annealing to the desired temperature, and then removing the film from its substrate to create a powder. Chemical signatures for

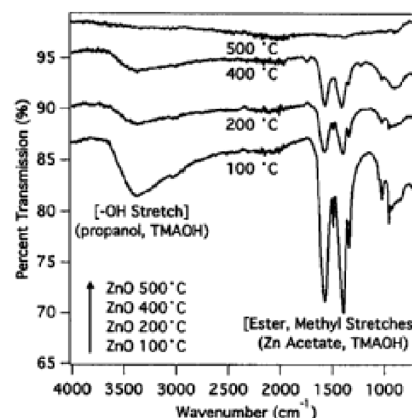


**Figure 3.** Fourier transform infrared spectroscopy (FTIR) spectra of ZnO films annealed at various temperatures between 100 and 500 C. The FTIR signature of the organic starting materials does not disappear until the film has been annealed over 400 C.

acetate (near 1400 and 1600 $cm^{-1}$), TMAOH (1300 and 1500 $cm^{-1}$), and the hydroxyl feature between 3000 and 3500 $cm^{-1}$ are clear indicators that the particle precursors remain in the film until very high annealing temperatures are attained. The critical temperature for removing chemical precursors from films appears to be 400 °C, above which little, if any, signal from precursor material is seen.

**Film Contraction.** In order to understand the effect annealing has on film contraction, film thickness and porosity were monitored as a function of annealing temperature. Both measurements show that below 400 °C there is little change in the film density; however over 400 °C. the film porosity rapidly decreases leading to a noticeable decrease in film thickness. The same samples at each temperature were used for XRD, for physical profilometry, and for ellipsometry for consistency.

Film thickness was measured using physical profilometry Sample thicknesses were measured five times before and after annealing in order to calculate the percentage change from the initial film thickness (see Figure 4 top). The error bars shown in Figure 4 are the standard deviation of the percentage change in film thickness. What is clearly seen is an initial decrease in film thickness (15%) that can be attributed to a loss of solvent. From 100 to 400 °C, there is a small decrease in film thickness (15% to 22%) that can be attributed to further losses of trapped solvent and precursor materials and to particle sintering. Between 400 and 500 °C, we see a rapid drop in film thickness (78% to 64% of original film thickness). This decrease is related to the film fully sintering and coincides with the film becoming densified. Between 500 and 800 °C, there is only a 4% loss of original film thickness that further demonstrates that the film is almost completely densified.

By monitoring the refractive index of the material, the degree of porosity can he calculated. As was demonstrated by Liu et al. and by Expert et al..[32,33] the complex refractive index can he determined using spectroscopic ellipsometry. By comparing the real part of the complex refractive index below the absorption onset to the known values for bulk ZnO. we can calculate the degree of porosity in the film. This assumes the material is a binary mixture of ZnO ($n_{600}$ = 1.96)[33] and air ($n_{600}$ = 1). The porosity ($P$) is then determined from the Bruggeman[34]

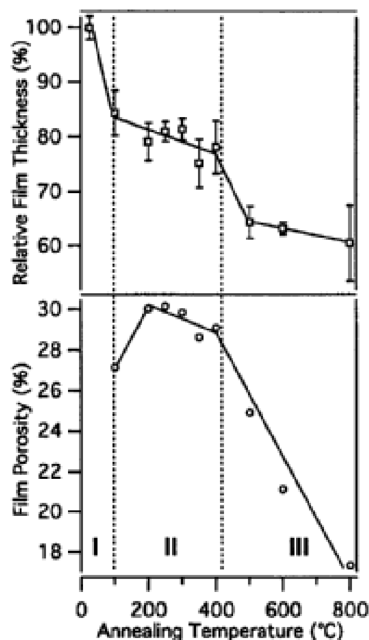


**Figure 4.** Change in ZnO film thickness (top) and porosity (bottom) versus thermal annealing temperature. Film thickness was determined using physical profilometry, porosity by ellipsometry.

model (eq 2), where neff and n, are the effective refractive indices of the porous film and bulk ZnO at 600 nm respectively.

$$P = 1 - \left(\frac{n_{\text{eff}}^2 - 1}{n_{\text{eff}}^2 + 2}\right) \Big/ \left(\frac{n_{\text{m}}^2 - 1}{n_{\text{m}}^2 + 2}\right) \quad (2)$$

Figure 4 (bottom) depicts the change in porosity of the ZnO film as a function of film annealing temperature. Below annealing temperatures of 400 °C, the film porosity is 30%. There is an initial increase in porosity between 100 and 200 °C that is consistent with the evaporation of 1-propanol. Above 400 °C, the porosity rapidly drops, indicating that the film is densifying. Above 500 °C, the porosity continues to decrease, indicating that the film has not fully contracted in the half hour annealing step.

**Electronic Properties.** Electron mobility was determined at a number of annealing temperatures from the transport curves of field-effect transistors (PET). For temperatures from 200 to 400 °C, the transistors behaved quadratically and the mobility was determined using eq 3.[35]

$$J_{\text{ds}} = \frac{\mu W C_i}{2L}(V_{\text{g}} - V_{\text{T}})^2 \quad (3)$$

Here $\mu$ is the electron mobility, $W$ the channel width, $C_i$ the capacitance of the dielectric layer, $L$ the channel length, $V_g$ the gate voltage, and $V^T$ the threshold voltage. However, for the samples prepared at 425 °C and higher, the transistors behaved linearly and the mobility was determined using eq 4.[35]

$$J_{\text{ds}} = \frac{\mu W C_i}{L}(V_{\text{g}} - V_{\text{T}})V_{\text{ds}} \quad (4)$$

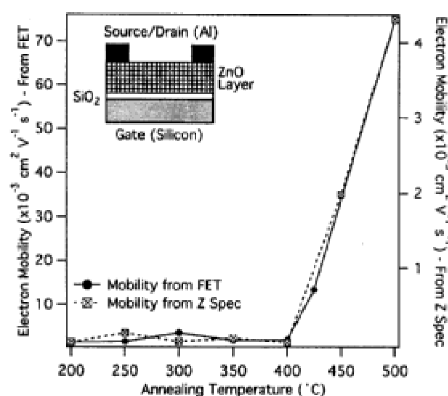


**Figure 5.** Average mobility, determined from field effect transistor transfer curves or the real component of the electrical impedance spectroscopy data. Inset shows FET device layout.

The determined mobility is plotted in Figure 5 and shows a clear dependence on annealing temperature. For each of the transport measurements, the drain voltage was maintained at 20 V. This range of temperatures was chosen because below 200 °C the channel resistance was too high to see FET behavior in the MIS-FET structure utilized. Above 500 °C, the channel resistance is sufficiently high that changes in gate voltage do not modulate the transport characteristics. Although other structures are available to measure the transport characteristics of films outside of this temperature range, fabrication of these devices was not necessary to understand ZnO densification and were thus not undertaken.

Electrical impedance measurements were also performed on ZnO sandwich structures at the same thermal annealing temperatures. ZnO was sandwiched between ITO and gold. Devices fabricated with either gold or aluminum electrodes exhibited similar impedance spectra. However, gold was chosen because the electrodes did not deteriorate in air. Impedance spectra were collected between 10 and $10^6$ Hz at applied voltages between 0 and 1 V. Two semicircular features were observed in the Nyquist plots for all temperature and voltage ranges measured. Impedance data are shown in the Supporting Information. These data show a clear resistance shift from low to high frequency as the sample is annealed.

Previous studies[36,37] have linked the low-frequency impedance component to conduction along the particle surface (or grain boundaries) while the high-frequency component is attributed to conduction through the particle core. We have confirmed this assertion by measuring a sample, prepared at 100 °C, before and after butane thiol treatment. Films passivated with butane thiol lack the low-frequency, surface component (see Supporting Information), indicating that this feature is related to conduction mediated by surface states. This indicates that for samples annealed at or below 400 °C, there is a significant resistance contribution from surface defects that, upon annealing over 400 °C, decreases substantially.

The data in the Bode plot were modeled as two Randles cells in series as shown in Chart 1. This model is consistent with the observed impedance data and with the work of Andres-Verges.[36] Here, each resistor represents the sum of the resistance across either the core or surface o f the particles and the corresponding

CHART 1

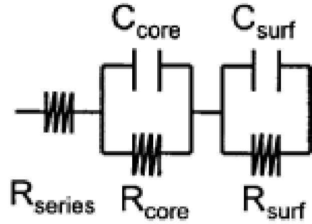


capacitors represent the capacitance of the film due to either the core or surface of the particles. At high frequencies, charge that becomes trapped in surface states will not contribute to the impedance of the film. At lower frequencies, charge interacts with the films longer and can trap and detrap from surface states within the voltage sweep of the measurement. The resistance of both the core, $R_{core}$, and the surface component, $R_{surf}$, can be determined using eq 5

$$\rho_{surf/core} = R_{surf/core} A/d \quad (5)$$

where $R_{surf/core}$ is the resistance calculated from the impedance data, A is the surface area of the device, and $d$ is the device thickness. The surface resistivity is plotted as a function of the annealing temperature in Figure 6. $R_{surf}$ is initially very high and remains so until 400 °C, above which temperature it drops substantially. This drop coincides with the densification of the film as seen in Figure 4. By contrast, the core resistivity ($R_{core}$) initially increases and remains high until the film fully densifies. This result is unexpected, as the crystallites are known to be growing in size throughout the temperature range measured, and increased crystallite size and crystallinity are known to lead to higher conductivity in ZnO films.

Following the work of Kassing,[38] the film mobility can be calculated using eq 6

$$\mu = d^2 f/2E \quad (6)$$

Here $d$ is the film thickness, $f$ is the frequency at which the real component of the impedance plateaus at low frequencies, and $E$ is the applied voltage (taken as 10 mV, the oscillation voltage).

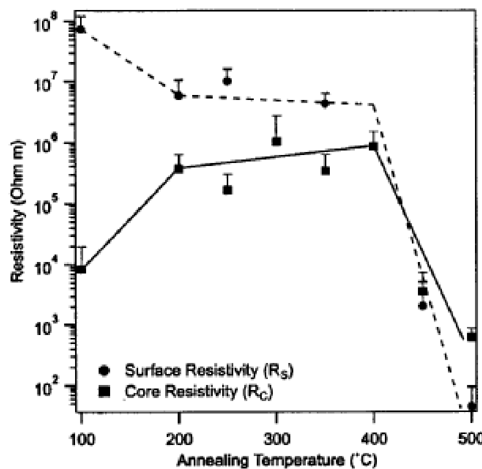


**Figure 6.** Surface and core resistivity as a function of the annealing temperature determined from electrical impedance measurements using a mode] composed of two Randles cells in series.

The mobility determined in this way is shown in Figure 5 and follows the same temperature trend as the FET-determined mobility, which also rapidly increases for $T_{ann}$. > 400 °C.

## Discussion

The results presented here clearly show that ZnO nanocrystal films densify above 400 °C, which we denote the densification temperature, $T_c$. There is high porosity below $T_c$, and a dramatic decrease in film thickness above this temperature. The electronic properties are also controlled by this porosity. Below the densification temperature, the surface resistivity is relatively steady, while the core resistivity initially increases up to $T_c$. and then remains steady. Above the densification temperature, both components decrease drastically.

These results impact directly on the electron mobility derived from FET devices. We see that for annealing temperatures $T_{ann}$, < 400 °C. the drain current increases quadratically with drain voltage; however, for $T_{ann}$, > 400 °C the drain current varies linearly. The mobility rapidly increases above the measurable limit of our FET structures for $T_{ann}$ > 500 °C. Interestingly, the mobility for T < 400 °C peaks near $T_{ann}$ = 300 °C at 0.04 $cm^2\ V^{-1}\ s^{-1}$ and then decreases to 0.02 $cm^2\ V^{-1}\ s^{-1}$ at $T_{ann}$ = 350 °C. This maximum before a minimum near $T_{ann}$ = 400 °C was observed consistently; the data presented in Figure 5 represent the average of four repeat series. This mobility-dip, as well as the resistance and mobility changes in impedance can be explained by comparing these results, with the observed thin-film absorption spectra in Figure 2a. This figure shows that the first excitonic peak is well-defined for as-cast films, because the particle size distribution is very narrow in solution and this does not change for lightly annealed samples. The first excitonic peak is also well-defined for samples annealed above the densification temperature, indicating that large crystallites with bulklike absorption are present. Between these temperatures. the absorption broadens, indicative of polydispersity in the film. For as-cast films, the mobility is very low, <$l0^{-4}$ $cm^2\ V^{-1}\ s^{-1}$, due to the high activation energy barrier for hopping between nanocrystals. This barrier will decrease with annealing, as nanocrystals sinter and insulating ligands are desorbed. which also reduces the thickness of the tunneling barrier between individual nanocrystals. This will drive an increase in mobility. However for quantized ZnO nanocrystals, this can be offset by the changes in the conduction band energy levels within the particles.[39,40] We expect the electron jump frequency from particle 1 to particle 2, $v1.2^e$, to be of the form

$$v_{1,2}^{\ e} = A e^{-(\Delta E_{act} + \Delta E_{1,2})/kT} \quad (6a$$

Here, is the "intrinsic" tunneling barrier between particle 1 and particle 2 due to the ligand barrier, while AE12 is a size- dependent term for transport between two neighboring crystallites of different size. As the nanocrystal film is annealed, ligands are removed and the tunneling distance between crystallites decreases. This reduces $\Delta E_{act}$. Sintering will also increase the electron mean free path, increasing the value of $A$ (Figure 7). Both effects would lead to an increase in carrier mobility, which contradicts observation. We attribute the decrease in mobility at intermediate temperatures to the polydispersity in the QDs that is caused by annealing. Norris[41] and colleagues have found evidence for size-dependent activation energies, $\Delta E^{1,2}$, for carrier transport through CdSe QD films. They attributed this to the dispersion in the energy levels in QDs in the strong

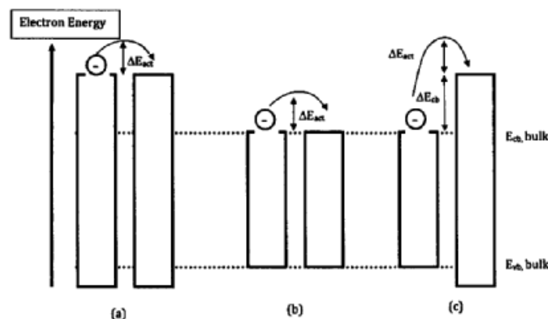


**Figure 7.** Schematic diagram showing comparative tunneling barriers for (a) quantized, as-cast films, (b) ZnO nanocrystal films with bulk band gap, and (c) intermediate case for polydisperse nanocrystal films. The hopping barrier is predicted to be largest for the polydisperse films, case c, since there is both a ligand tunneling barrier and an additional barrier due to differences in conduction band levels in neighboring particles.

confinement regime. Vanmaekelbergh[42] and co-workers studied ZnO QD film conductivity and also found size-dependent activation energies. They suggested that Coulomb charging was the major cause of this effect. Both mechanisms are consistent with our experimental data, since both mechanisms will produce enhanced activation energies for transport from small to large QDs. The effect of this is that charge carriers will tend to be isolated on the larger crystallites in the film. This reduces the number of pathways through the film and reduces the conductivity. This effect manifests itself most strongly at intermediate temperatures. Higher annealing temperatures increase the average size of the crystallites such that the size-dependent activation energy disappears. The mobility-dip can be accounted for this way. These results are contrary to those of Liu,[43] who found there was a very limited effect on mobility when two distinct particle sizes were mixed. However, unlike the PbSe films studied by Liu, our semiconductor films are composed of particles that are spun with low polydispersity and are then annealed. The influence of quantum size effects on electrical conductivity will be evident only when the energy barrier due to the size effect is larger than the intrinsic ligand-induced barrier. For ligand-protected samples studied at room temperature, the ligand-induced tunneling barrier will dominate, and size effects may be difficult to discern.

## Conclusions

We have demonstrated that semiconducting ZnO nanocrystals can be used to fabricate solution-processable thin films. The materials are n-type, moderately doped when annealed in nitrogen, and exhibit reasonable mobilities at low annealing temperatures. The nanocrystal inks are superior to sol—gel routes for low temperature fabrication. We find that crystallite size is constant until 400 °C and then increases throughout the annealing range between 400 and 800 °C. The electronic properties are limited by surface states and remain unchanged while the film is still porous. The impedance data prove that there is substantial surface state mediated conduction for films that are sintered at <400 °C. Importantly, however, we find that surface states can be passivated by ligands, which may provide an important mechanism for achieving high performance films annealed at low temperatures.

**Acknowledgment.** The authors thank the ARC for support under Grant DPI 09485.

**Supporting Information Available:** Plots of impedance measurements, representative transport curves, and output curves. This information is available free of charge via the Internet at http://pubs.acs.org.

## References and Notes

(1) Anderson, N. A.; Lian, T. Q. Ultrafast electron transfer at the molecule-semiconductor nanoparticle interface. Annu. Rev. Ph vs. Chem. **2005**, 56, 491—5 19.

(2) Shipway, A. N.; Katz. E.; Wilner, 1. Nanoparticle arrays on surfaces for electronic, optical, and sensor applications. ChemPhysChe,n **2000**, 1 (1), 18—52.

(3) Trindade, T.; O'Brien, P.: Pickett. N. L. Nanocrystalline semiconductors: Synthesis, properties, and perspectives. Che,n. e'.Jater. **2001**, 13 (Ii), 3843—3858.

(4) Gur. 1.; Fromer. N. A.; Geier, M. L.; Alivisatos, A. P. Air-stable all-inorganic nanocrystal solar cells processed from solution. Science **2005**, 310, 462—465.

(5) Luther. 3. M.: Law, M.: Beard, M. C.; Song. Q.; Reese, M. 0.: Ellingson, R. J.: Nozik. A. J. Schottky solar cells based on colloidal nanociystal films. Nano Let!. **2008**, 8 (10), 3488—3492.

(6) Mashford, B. S.; Nguyen, T. L.; Wilson, G. J.: Mulvaney, P. All-inorganic quantum-dot light-emitting devices formed via low-cost, wet-chemical processing. J. Mater. Chem. . 20 (fl, 167—172.

(7) Ong, B. S.; Li, C. S.: Li, Y. N.; Wu, Y. L.: Loutfy, R. Stable, solution-processed, high-mobility ZnO thin-film transistors. J. Am. Chem. Soc. **2007**, 129 (10), 2750.

(8) Wu, Y. L.; Li, Y. N.; Liu, P.; Gardner. S.; Ong, B. S. Studies of gold nanoparticles as precursors to printed conductive features for thin-film transistors. Chem. Mater. **2006**, 18 (19), 4627—4632.

(9) Hench, L. L.; West, J. K. The sol-gel process. Chern. Rev. **1990**. 90 (1), 33—72.

(10) Ozgur, U.; Alivov, Y. I.; Liu, C.; Teke, A.; Reshchikov, M. A.; Dogan, S.: Avrutin. V.: Cho, S. J.; Morkoc, H. A comprehensive review of ZnO materials and devices. J. App!. Phys. **2005**, 98, (4).

(11) Bashir, A.; Wobkenberg, P. H.; Smith, 3.; Ball. J. M.; Adamopoulos, 0.: Bradley, 0. D. C.; Anthopoulos, T. D. High-performance zinc oxide transistors and circuits fabricated by spray pyrolysis in ambient atmosphere. Adi'. Mater. **2009**. 21(21), 2226.

(12) Boesen, G. F,: Jacobs. J. E. ZnO field-effect transistor. Proc. Inst. Elecir. Electron. Eng. **1968**, 56 (11), 2094.

(13) Carcia, P. F.; McLean, R. S.; Reilly, M. H.; Nunes, 0. Transparent ZnO thin-film transistor fabricated by rf magnetron sputtering. App!. Phys. Lett. **2003**,82(7). 1117—1119.

(14) Ohya, Y.; Niwa, T.: Ban, T.; Takahashi, Y. Thin film transistor of ZnO fabricated by chemical solution deposition. Jpn. J. App!. Phys., Part 1 **2001**, 40 (1), 297—298.

(15) Sun. B.; Sirrioghaus. H. Solution-processed zinc oxide field-effect transistors based on self-assembly of colloidal nanorods. Nano Left. **2005**, 5 (12), 2408—2413.

(16) Yoo, 3. B.: Fahrenhruch, A. L.; Bube, R. H. Transport mechanisms in ZnO-CdS-CuInSe2 solar-cells. J. App!. Phys. **1990**, 68 (9), 4694—4699.

(17) Beck. V. J. H.; Wienk, M. M.; Janssen, R. A. J. Efficient hybrid solar cells from zinc oxide nanoparticles and a conjugated polymer. Adu. Mater. **2004**. .16 (12), 1009—+.

(18) Ohta, H.; Orita, M.; Hirano, M.: Hosono, H. Fabrication and characterization of ultraviolet-emitting diodes composed of transparent p-n heterojunction, p-SrCuzO2 and n-ZnO. J. App!. Phys. **2001**, 89(10). 5720— 5725.

(19) Pearton, S. J.; Norton, D. P.: Ip, K.; Heo. Y. NV.; Steiner, T. Recent advances in processing of ZoO. J. Vac. Sci. Technol., B **2004,** 22, 932—948.

(20) Wang, Z. L. Zinc oxide nanostructures: growth. properties and applications. J. Phys.: Condens. Matter **2004**, 16 (25), R829•-R858.

(21) Meulenkamp, H. A. Synthesis and growth of ZnO nanoparticles. J. Phys. Chem. B **1998**, 102 (29), 5566—5572.

(22) Spanhel. L.: Anderson, M. A. Semiconductor clusters in the sot-gel process—quantized aggregation, gelation, and crystal-growth in concentrated ZnO colloids. J. Am, Chem. Soc. **1991**, 113 (8), 2826-2833.

(23) Patterson, A. L. The Scherrer formula for X-ray particle size detennination. Phys. Rev. .**1939**, 56 (101, 978—982.

(24) Enzo, S.; Polizzi. S.; Benedetti, A. Applications of fitting techniques to the Warren—Averbach method for X-ray-line broadening analysis. Z. Kristallogr. **1985**, 170 (1—4), 275—287.

(25) Swanson, H.; Fuyat, R. Standard X-ray diffraction patterns. Nat!. Bur. Stand. Circ. (U.S.) **1953**, 539, (2).

(26) Wood, A.; Giersig, M.; Hilgendorff, M.; Vilas-Campos, A.: LizMarzan, L. M.; Mulvaney, P. Size effects in ZnO: The cluster to quantum dot transition. Aust. J. Chem. **2003**, 56(10), 105 1—1057.

(27) Rossetti, R.; Ellison, J. L.; Gibson, J. M.; Brus, L. E. Size effects in the excited electronic states of small colloidal CdS crystallites. J. Chem. Phys. **1984**, 80 (9), 4464-4469.

(28) Koch, U.; Fojtik, A.; Weller, H.; Flenglein, A. Photochemistiy of semiconductor colloids 0.13. preparation of extremely small ZnO particles, fluorescence phenomena and size quantization effects. Che,n. Ph3’s. Lea.
**1985**, 122 (5), 507—510.

(29) Kroger, F. A.; Vink, H. J. The origin of the fluorescence in self-activated ZnS, CdS, and ZnO. J. them. Ph3’s. **1954**, 22 (2), 250—252.

(30) Mollwo, E. Die Wirkung von Wasserstoff auf die Leitfahigkeit und Lumineszenz von Zinkoxydkristallen. Z. Phys. **1954**, 138 (3—4), 478—488.

(31) Norberg, N. S.; Gamelin. D. R. Influence of surface modification on the luminescence of colloidal ZnO nanocrystals. J. Phys. Chein. B **2005**, 109 (44), 20810—20816.

(32) Eypert, C.; Znaidi, L. Spectroscopic ellipsometry study of ZnO thin films. Horiba Jobin Yvon Application Note **2004**. 2 Oplical Coatings, (SE 12).

(33) List. Y. C.; Hsieh. J. H.: Tung. S. K. Extraction of optical constants of zinc oxide thin films by ellipsometry with various models. Thin Solid Films **2006**, 510(1—2), 32—38.

(34) Bruggeman, D. A. G. Calculation of various physics constants in heterogenous substances. 1. Dielectricity Constants and conductivity of mixed bodies from isotropic substances. Ann. Phys. **1935**, 24 (7), 636—664.

(35) Sze, S.; Ng, K. Physics of Semiconductor Devices, 3rd ed.: Wileylnterscience: Hoboken, NJ, **2007**: p 815.

(36) Andres-Verges, M.; West. A. R. Impedance and modulus spectroscopy of ZnO varistors. J. Electroceram. **1997**, 1(2), 125—132.

(37) Nan, C. W.: Tschope, A.: Holten, S.: Kliem, H.; Birringer, R. Grain size-dependent electrical properties of nanocrystalline ZnO..1. Appi. Phys.
**1999**, 85 (11), 7735—7740.

(38) Kassing, R. Calculation of frequency-dependence of admittance of SCLC diodes. Phys. Status Solidi A **1975**, 28 (1), 107—117.

(39) Brus, L. Electronic wave-functions in semiconductor clusters—-expertinent and theory. J. Phys. C/tern. **1986**. 90 (12), 2555—2560.

(40) Viswanatha, R.: Sapra, S.; Satpati, B.: Satyam, P. V.: l)ev, B. N.: Sarma, D. D. Understanding the quantum size effects in ZnO nanocrystals.
J. Mater. Cheni. **2004**, 14 (4). 661—668.

(41) Kang. M. S.: Sahu. A.: Norris, 1). 1.: Frisbie, C. I). Size-dependent electrical transport in CdSe nanocrystal thin films. Nano Leti. **2010**. 10(9),
3727—3732.

(42) Roest, A. L.; Kelly, J. J.: Vanmaekelbergh. I). Coulomb blockade of electron transport in a ZnO quantum-dot solid. Appi. Phys. Lett. **2003**, 83 (26), 5530—5532.

(43) Liu, Y.; Gibbs, M.: Puthussery, J.: Gaik. S.; Ihly. R.; Hillhousc. H. W.; Law, lvi. Dependence of canier mobility on nanocrystal size and ligand lenath in PbSe nanocrystal solids. Nano LeIt. **2010**, 10 (5). 1960—1969.

JP107043Z